



Alteration of the subducting oceanic lithosphere at the southern central Chile trench–outer rise

Eduardo Contreras-Reyes, Ingo Grevemeyer, Ernst R. Flueh, and Martin Scherwath

*Leibniz-Institute of Marine Sciences (IFM-GEOMAR), Wischhofstrasse 1-3, D-24148 Kiel, Germany
(econtreras-reyes@ifm-geomar.de; igrevemeyer@ifm-geomar.de; eflueh@ifm-geomar.de; mscherwath@ifm-geomar.de)*

Martin Heesemann

*Department of Earth Sciences, University of Bremen, Postfach 330440, D-28334 Bremen, Germany
(heesema@uni-bremen.de)*

[1] Hydrothermal circulation and brittle faulting processes affecting the oceanic lithosphere are usually confined to the upper crust for oceanic lithosphere created at intermediate to fast spreading rates. Lower crust and mantle rocks are therefore relatively dry and undeformed. However, recent studies at subduction zones suggest that hydration of the oceanic plate is most vigorous at the trench–outer rise, where extensional bending-related faulting affects the hydrogeology of the oceanic crust and mantle. To understand the degree of hydration, we studied the seismic velocity structure of the incoming Nazca plate offshore of southern central Chile ($\sim 43^{\circ}\text{S}$); here the deep-sea trench is heavily filled with up to 2 km of sediments. Seismic refraction and wide-angle data, complemented by seismic reflection imaging of sediments, are used to derive a two-dimensional velocity model using joint refraction and reflection traveltime tomography. The seismic profile runs perpendicular to the spreading ridge and trench axes. The velocity model derived from the tomography inversion consists of a ~ 5.3 -km-thick oceanic crust and shows P wave velocities typical for mature fast spreading crust in the seaward section of the profile, with uppermost mantle velocities as fast as ~ 8.3 km/s. Approaching the Chile trench, seismic velocities are significantly reduced, however, suggesting that the structures of both the oceanic crust and uppermost mantle have been altered, possibly due to a certain degree of fracturing and hydration. The decrease of the velocities roughly starts at the outer rise, ~ 120 km from the deformation front, and continues into the trench. Even though the trench is filled with sediment, basement outcrops in the outer rise frequently pierce the sedimentary blanket. Anomalously low heat flow values near outcropping basement highs indicate an efficient inflow of cold seawater into the oceanic crust. Hydration and crustal cracks activated by extensional bending-related faulting are suggested to govern the reduced velocities in the vicinity of the trench. Considering typical flow distances of 50 km, water might be redistributed over most of the trench–outer rise area. Where trapped in faults, seawater may migrate down to mantle depth, causing up to $\sim 9\%$ of serpentinization in at least the uppermost ~ 2 km of the mantle between the outer rise and the trench axis.

Components: 10,027 words, 9 figures.

Keywords: trench–outer rise; bending-related faulting; seismic tomography.

Index Terms: 8170 Tectonophysics: Subduction zone processes (1031, 3060, 3613, 8413); 8150 Tectonophysics: Plate boundary: general (3040); 7220 Seismology: Oceanic crust.

Received 15 March 2007; **Accepted** 4 May 2007; **Published** 7 July 2007.

Contreras-Reyes, E., I. Grevemeyer, E. R. Flueh, M. Scherwath, and M. Heesemann (2007), Alteration of the subducting oceanic lithosphere at the southern central Chile trench–outer rise, *Geochem. Geophys. Geosyst.*, 8, Q07003, doi:10.1029/2007GC001632.

1. Introduction

[2] Oceanic lithosphere created at moderate to fast spreading mid-ocean ridges is characterized by a ridge-parallel fault pattern. Pervasive fracturing and hydrothermal activity, however, are largely confined to crustal levels [e.g., *Carbotte and Scheirer*, 2004; *Karson*, 1998]. As the crust ages, cracks and pore spaces inherently related to the formation of crust are clogged by precipitation of secondary hydrothermal alteration products in the extrusive lava pile [e.g., *Alt et al.*, 1986; *Wilkins et al.*, 1991; *Grevemeyer and Bartetzko*, 2004]. Global compilations of seismic refraction velocities for the uppermost oceanic crust [*Grevemeyer and Weigel*, 1996; *Carlson*, 1998] and dedicated seismic refraction experiments [e.g., *Grevemeyer and Weigel*, 1997; *Grevemeyer et al.*, 1999] have established an empirical relationship between lithospheric age and seismic velocity. The global trend suggests that uppermost P wave velocities of layer 2 increase rapidly close to the spreading axis and within ~8 Ma reach values of mature oceanic crust (>4.5 km/s) [*Carlson*, 1998; *Grevemeyer and Bartetzko*, 2004]. Within this context, we will refer to “normal” mature oceanic lithosphere typical of fast spreading structures if (1) hydration is confined to the permeable upper lava pile, (2) the ridge flank hydrothermal circulation system has largely ceased, and (3) the oceanic lithosphere is positioned away from anomalous regions such as fracture zones and hot spots regions [e.g., *White et al.*, 1992].

[3] Growing observational evidence in subduction zones suggest that this condition of “normal” and “unaltered” ocean lithosphere can be dramatically perturbed at the outer rise seaward of deep-sea trenches [e.g., *Peacock*, 2004; *Ranero et al.*, 2003]. The outer rise is formed when the ocean lithosphere approaches a subduction zone and bends into the trench, thus producing a prominent outer bulge seaward of the trench axis. Here, outer rise earthquakes are linked to bending-related normal faulting [*Chapple and Forsyth*, 1979] and possibly rupture the oceanic mantle [e.g., *Kanamori*, 1971; *Christensen and Ruff*, 1983], creating a pervasive tectonic fabric that may cut across the crust,

penetrating deep into the uppermost mantle [e.g., *Peacock*, 2001; *Ranero et al.*, 2003]. Moreover, new crustal cracks and fissures are caused by bending-related faulting seaward of the trench axis, modifying the structure of the crust. Therefore bending-related faulting plays a crucial role for the alteration of oceanic lithosphere; it affects the porosity and permeability structure of the entire oceanic crust and consequently generates pathways for fluids down to mantle depth.

[4] One key factor controlling the local hydrogeological regime of the oceanic lithosphere is the thickness of the sedimentary blanket. Convergent margins such as Central America and north Chile are poorly sedimented, and seawater can easily enter the igneous oceanic crust where the permeable basement rocks are widely exposed (e.g., surface-cutting tectonic faults or outcropping basement highs). These subduction zones have been suggested to be characterized by a high degree of hydration at the outer rise [*Ranero et al.*, 2003; *Ranero and Sallares*, 2004; *Grevemeyer et al.*, 2005, 2007]. In contrast, in well sedimented margins (Cascadia and southern central Chile), a thick sedimentary cover is believed to hinder interaction between the ocean and the basement. Therefore the degree of hydration is expected to be lower than in poorly sedimented trenches, although mechanisms by which fluids may bypass thick sediments remain still under debate. In general, the hydrothermal activity in the oceanic crust is controlled by faulting and the presence of outcropping basement highs. Heat flow data suggest that hydrothermal circulation is more vigorous at trenches where bending-related normal faults breach the seafloor and thus facilitate fluid flow into the crust [*Grevemeyer et al.*, 2005]. Outcropping basement also play a crucial role, since it may act as transmissive pathway for fluids and heat in areas where the surrounding basement is blanketed by sediments, as it has been evidenced by anomalous low heat flow values near seamounts, indicating an efficient inflow of cold seawater into the oceanic crust [*Villinger et al.*, 2002; *Fisher et al.*, 2003a, 2003b]. Isolated basement outcrops penetrating through thick sediments might guide hydrothermal circulation between sites separated by large distances [*Fisher et al.*, 2003a]. Once cold seawater

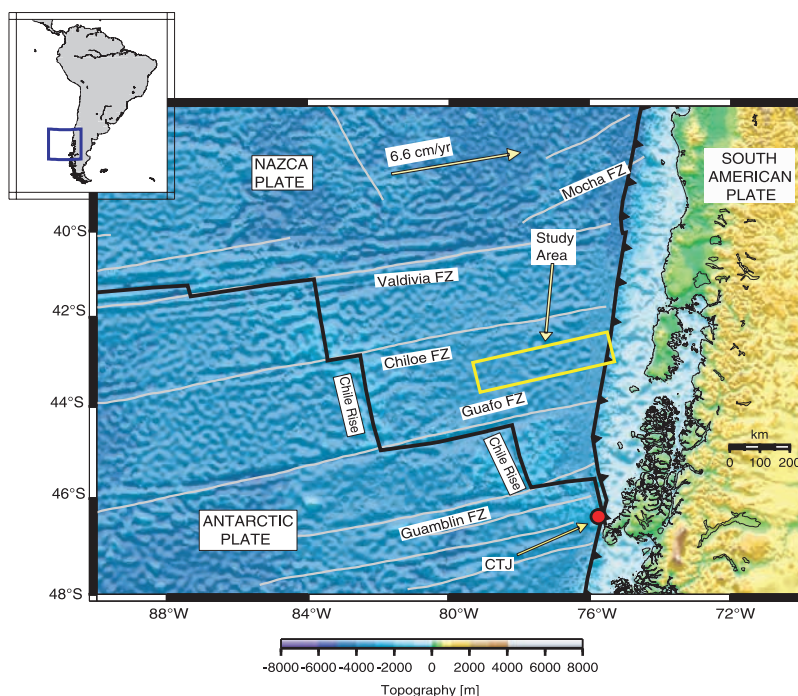


Figure 1. Geodynamic setting of Nazca, Antarctic, and South American plates. These plates join at the Chile Triple Junction (CTJ), where the Chile Rise is currently subducting at $\sim 46.5^{\circ}\text{S}$. The oceanic Nazca plate is segmented by several fracture zones (FZs), resulting in a strong variability of the age of the subducting plate. The study area is located between two Fracture Zones, Chiloe FZ and Guafo FZ, and its plate age ranges from 18.5 to 10 Ma along the Chile trench.

is infiltrated and bounded in the upper oceanic crust, tectonic faulting may allow fluids trapped within crustal pores spaces to enter the lower crust and perhaps even the upper mantle [e.g., Grevemeyer *et al.*, 2005].

[5] To better understand the transition from “normal” and “dry” to deformed and hydrated subducting lithosphere and its degree of hydration in the trench–outer rise area, we studied the velocity structure of the incoming oceanic Nazca plate offshore of south central Chile. Seismic wide-angle reflection and refraction data are used to derive an accurate 2-D tomography velocity model of a ~ 250 km long seismic profile located oceanward from the Chile trench axis. We present new geophysical evidence documenting changes in the seismic structure of the incoming oceanic plate from the outer rise to just before its subduction in the deep-sea trench. A nonlinear Monte Carlo uncertainty analysis is performed to estimate a posteriori model variance of the tomography velocity model. In addition, heat flow data recorded at the outer rise are used to study the distribution of temperature along the sediment/crust boundary. The data were acquired during the R/V *Sonne* cruise SO181 as part of the TIPTEQ (from The Incoming

Plate to Mega-thrust Earthquake processes) project [Flueh and Grevemeyer, 2005].

2. Tectonic Setting

[6] Along the south central Chile trench the southern Nazca plate subducts at a relatively high convergence rate of ~ 6.6 cm/yr beneath the South American plate, with a convergence azimuth of $\sim 78^{\circ}\text{E}$ [Angermann *et al.*, 1999] (Figure 1). The southern Nazca plate has been formed at the Chile Rise (a fast mid-ocean spreading ridge). Fracture zones (FZs) cut the Chile Rise into several segments (Figure 1), resulting in abrupt changes of thermal states along the plate boundary. The spreading center segments bounded by these fracture zones are roughly parallel to the trench strike (Figure 1). At $\sim 46.5^{\circ}\text{S}$ the Chile Rise is currently subducting, defining the Chile Triple Junction (CTJ) of the subducting Nazca and Antarctic plates, and the continental South American plate. North of the CTJ occur a series of age jumps across several fracture zones, from 0 Myr up to 18.5 Myr at the Valdivia FZ (Figure 1). The south central Chile trench is filled by terrigenous sediments sourced from the Andes [Thornburg and Kulm,

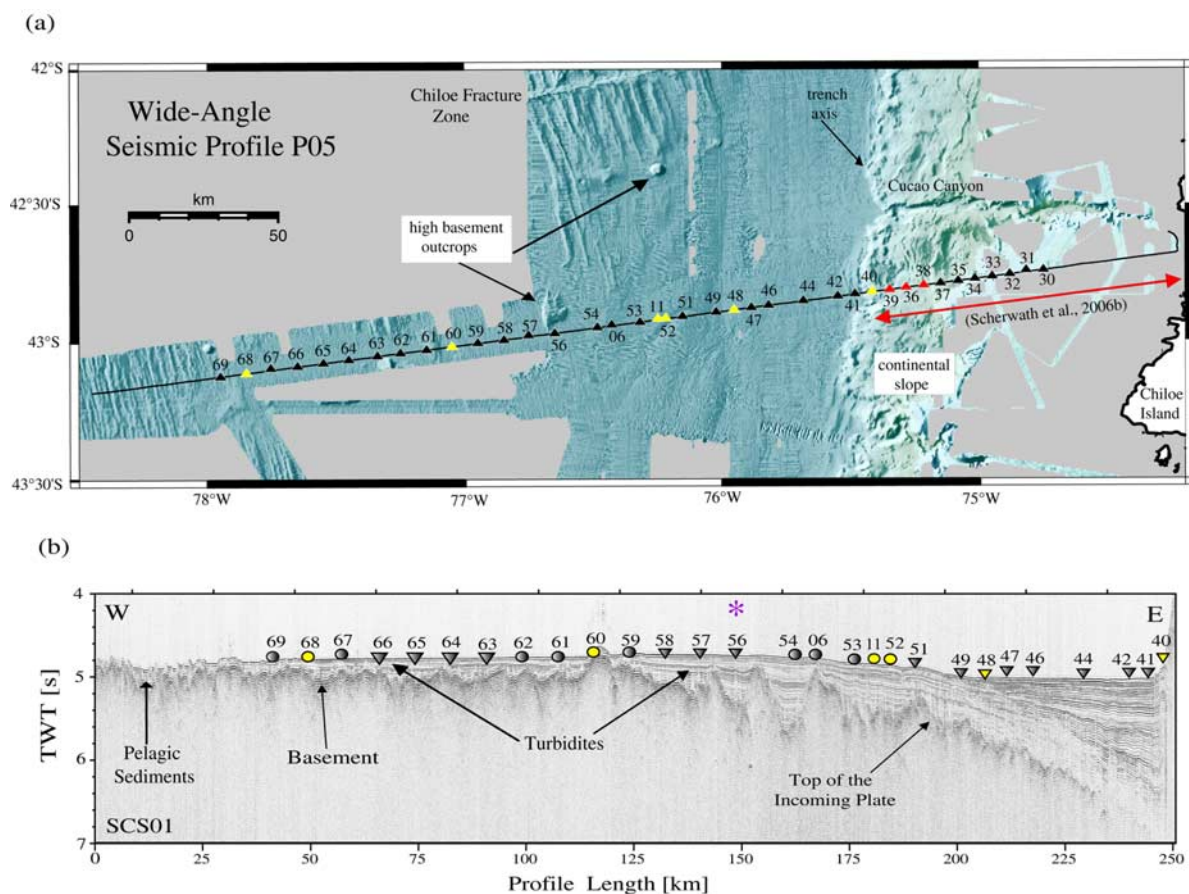


Figure 2. (a) High-resolution bathymetric image and wide-angle seismic profile P05. The seismic line begins ~ 280 km from the Chile Rise (see Figure 1), and it extends up to the deep-sea trench and part of the continental slope. Yellow triangles indicate the six stations of which data examples are shown in Figures 3 and 8. Red dots indicate the three stations positioned on the continental slope [Scherwath *et al.*, 2006b], which are included in our tomographic model. (b) High-resolution seismic line SCS01 coincident with wide-angle seismic profile P05. Locations of OBH are shown by solid circles, and locations of OBS are shown by solid triangles. Location of the high basement outcrop is denoted by asterisk. Some tensional normal faults are reflected by offsets in the trench–outer rise region.

1987]. Sediment within the trench are redistributed from south to the north [Thornburg *et al.*, 1990], which is explained by the slight northward dip of the trench floor [e.g., Thornburg *et al.*, 1990]. Trench fans (33–41°S) are built at the mouths of major submarine canyons and channels which act as point sources of sediment supply [Thornburg and Kulm, 1987]. South of 41°S, sheet turbidites extend across the entire width of the trench [Thornburg and Kulm, 1987].

[7] The westward terminus of the seismic wide-angle profile studied here is located approximately 280 km eastward of the Chile Rise on 9 Myr old crust [Tebbens *et al.*, 1997], the line orientation being parallel to the plate motion vector (Figure 1). The profile is located between Chiloe and Guafo FZs (Figure 1), where the plate age decrease from 18.5 to 10 Myr along the Chile trench, and the half-

spreading rate ranges between 45 and 35 mm/yr [Tebbens *et al.*, 1997]. The trench basin is broad, owing to the large extension of turbidite deposits seaward [Voelker *et al.*, 2006]. Further to the west, the Nazca plate is covered by a few hundred meters of hemipelagic and pelagic sediments, whereas toward the trench, the sedimentary cover becomes thicker due to the turbiditic deposits filling the trench with a total thickness of ~ 2 km [Scherwath *et al.*, 2006a]. The continental slope is steep and is characterized by the presence of the submarine Cucao Canyon (Figure 2a), while the continental shelf is broad and probably trapped large volume of Pliocene sediments [Reichert *et al.*, 2002].

3. Seismic Data

[8] From December 2004 to February 2005, the TIPTEQ project investigated the subduction zone

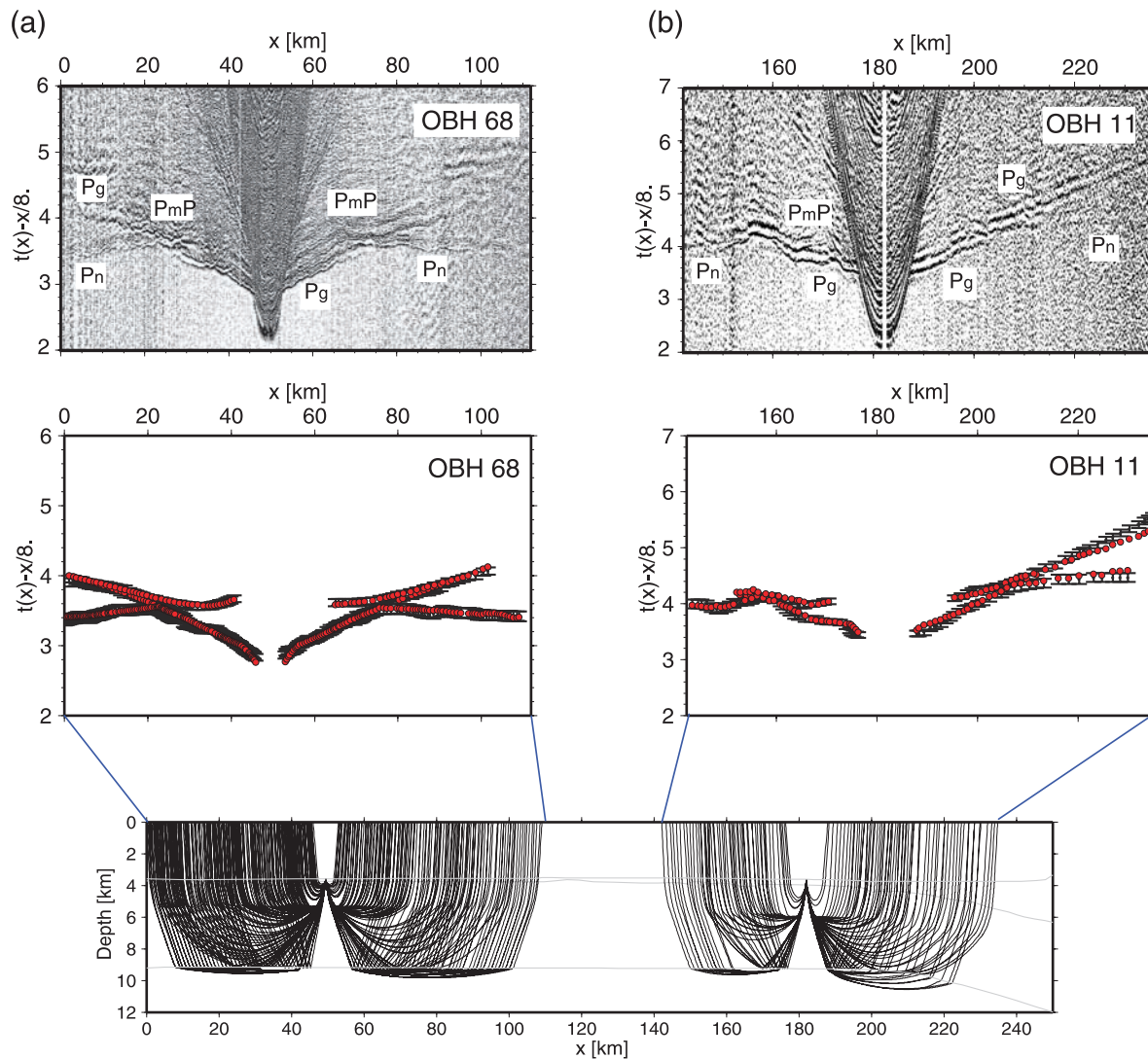


Figure 3. Examples of wide-angle seismic data with picked (solid circle with pick error) and predicted (red circles) traveltimes. Calculated traveltimes are based on the velocity model presented in Figure 7a, and corresponding raypaths are also plotted at the bottom. (a) OBH 68, (b) OBH 11, (c) OBH 60, (d) OBH 48, and (e) OBH 40.

offshore south-central Chile between 35° and 48°S aboard of the German R/V *Sonne*. During the cruise seismic wide-angle reflection and refraction data, high-resolution seismic reflection data, multi-beam bathymetry, heat flow, and seismological data were acquired in this region [Flueh and Grevemeyer, 2005; Scherwath *et al.*, 2006a] to study the physical properties of the incoming Nazca plate and its impact on seismogenesis, offshore of the rupture area of the 1960 Chile megathrust earthquake. In this paper, we present seismic wide-angle data that were collected along the profile P05 located seaward of the trench axis on the oceanic Nazca plate, supplemented by high-

resolution swath bathymetric images of the surrounding seafloor (Figure 2a). Shots were recorded with 38 OBS (Ocean Bottom Seismometers) [Bialas and Flueh, 1999] and OBH (Ocean Bottom Hydrophones) [Flueh and Bialas, 1996] spaced at a distance of ~5.5 km. Coincident seismic reflection data were also collected along this profile (Figure 2b). For the reflection investigation a 100-m-long 16-channel streamer and a Generator/Injector (GI) gun with a volume of 1.5 liters were used, providing high-resolution images of the sedimentary sequences blanketing the incoming plate. From the 38 seismic ocean bottom stations, 28 were deployed on the oceanic plate and the rest

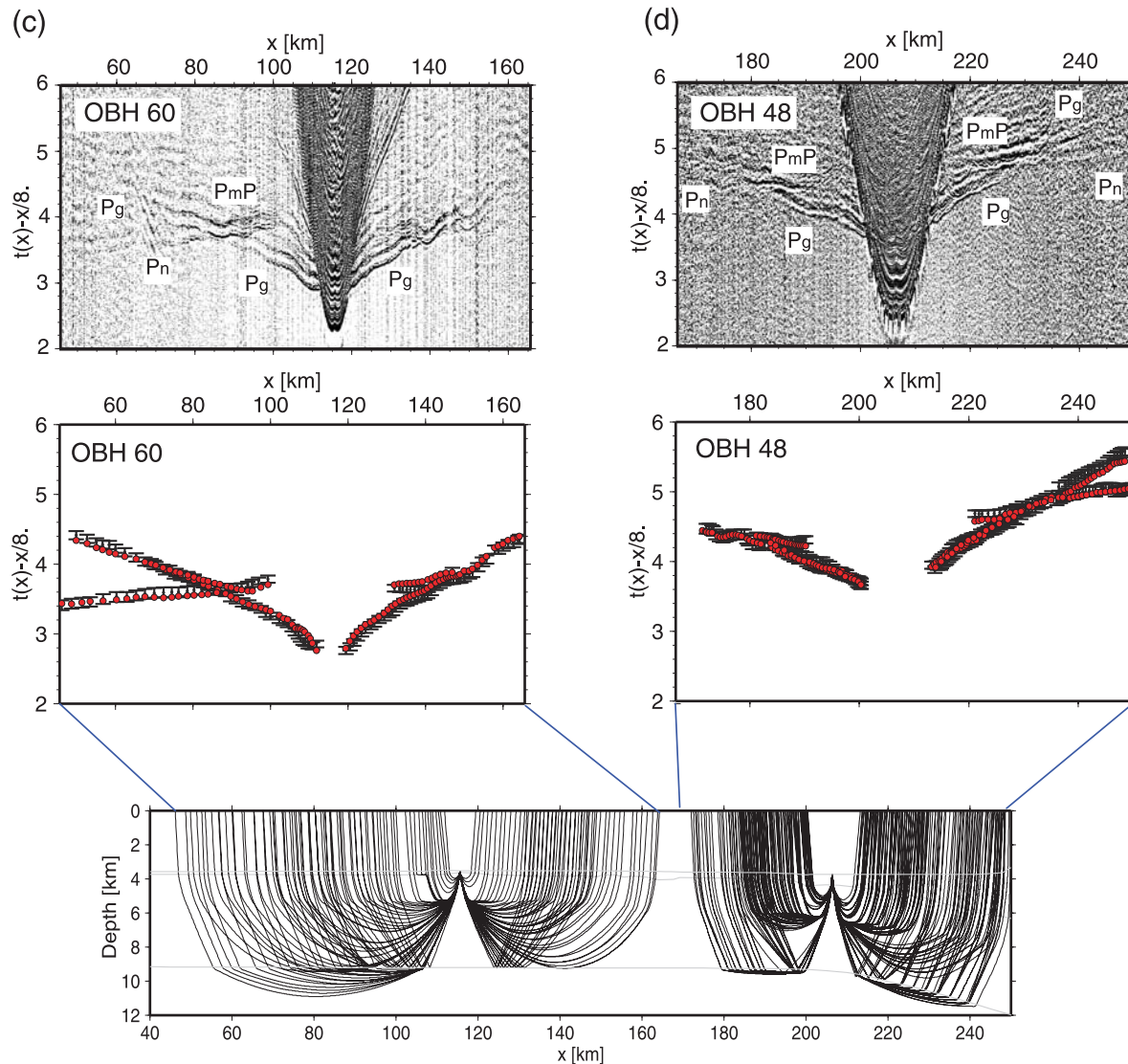


Figure 3. (continued)

along the continental slope. In order to study the seismic structure of the oceanic Nazca plate, we used the OBH/S deployed seaward of the trench. Three stations on the continental slope were also included in the inversion approach to constrain the velocity structure and Moho depth below the trench (see Figure 2a).

[9] The seismic source for the refraction work was a cluster of 8x8-liters G-guns, providing a total volume of 64 liters for each shot. This source was fired at a time interval of 60 s, which corresponds to an average shot spacing of ~ 150 m. The record sections were interpreted after bandpass filtering and predictive deconvolution. The signal-to-noise ratio obtained for most of the stations is high

(Figure 3). Crustal refractions (P_g), Moho reflections (P_mP) and upper mantle refractions (P_n) were recorded on almost all stations with excellent quality. Five examples of seismic record sections are shown in Figure 3, with their respective seismic phases identified. Apparent velocities, which are influenced by the trench-sediment, decrease toward the trench. Refractions through trench-sediment (P_s), and reflections from the top of the igneous crust (P_bP) start to appear at approximately profile-km 200 and hence 50 km from the trench axis. Figure 3e shows P_s and P_bP of good quality at OBH 40 at the trench. Those traveltimes complement the high-resolution seismic reflection data

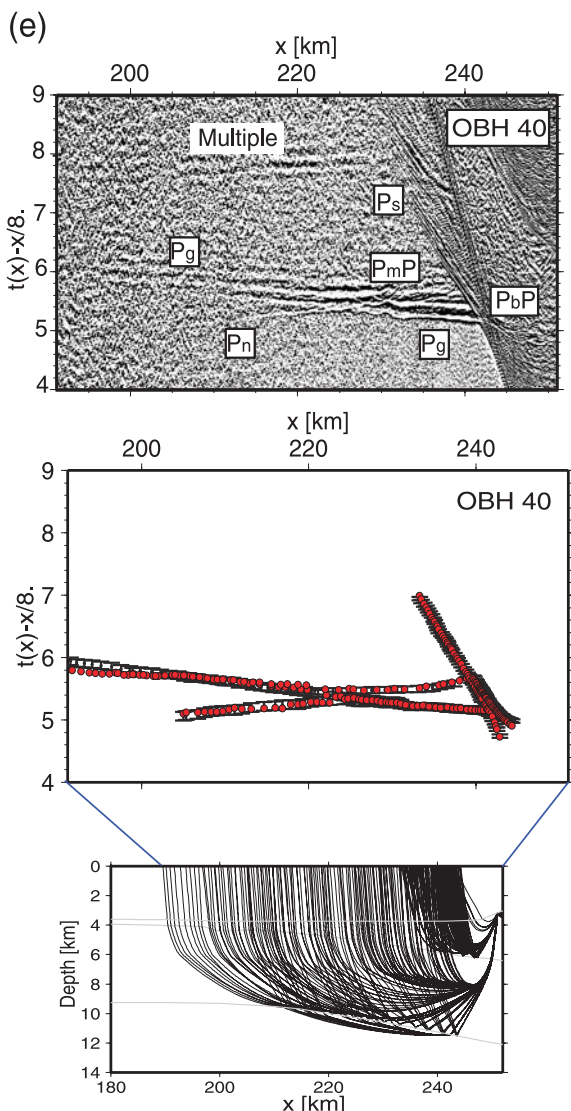


Figure 3. (continued)

(Figure 2b) and are used to constrain the sedimentary section in this part of the model.

[10] Picking of the seismic phases was done manually, and picking errors were assigned on the basis of the dominant period of the phase. A total of 5048 first arrivals (P_g and P_n), and 1721 Moho reflections (P_mP) were picked from 31 record sections. For the sedimentary section only stations located to the east of $x = 200$ km were utilized, because clear P_s and P_bP phases are confined to the trench basin. A total of 1456 P_s and 654 P_bP were picked from these stations. Typically, errors were assumed to be half a period of one arrival, to account for a possible systematic shift in the arrival identification, and were weighted according to the

phase quality. Average picking uncertainties are ~ 50 ms at near offsets and ~ 70 ms at far offsets for refracted arrivals, and ~ 50 ms and ~ 70 ms for P_bP and P_mP phases, respectively.

4. Traveltime Tomography Scheme

[11] The velocity-depth model was derived using the joint refraction and reflection traveltime inversion method of *Korenaga et al.* [2000]. This method allows simultaneous refraction and reflection traveltimes inversion for a 2-D velocity field that is parameterized as a sheared mesh hanging beneath the seafloor and where node spacings can vary laterally and vertically. The floating reflector is represented as an array of linear segments whose nodal spacing is independent of that used in the velocity grid and it has just one degree of freedom (vertical direction). Traveltimes and raypaths are calculated by utilizing a hybrid ray-tracing scheme based on the graph method and local ray-bending refinement [*van Avendonk et al.*, 1998]. Smoothing constraints using predefined correlation lengths (average-smoothness window) and optimized damping constraints for the model parameters are employed to regularize an iterative linearized inversion [*Korenaga et al.*, 2000]. We use a hybrid approach of multistep tomography using four layers, (1) water, (2) sedimentary section, (3) oceanic crust, and (4) upper mantle. To derive the velocity depth model, the water depths were taken from the multi-beam bathymetry, which remained fixed during the inversion. The vertical incidence reflection data, sediment refracted P_s and reflected P_bP phases were used to invert for the velocities and thickness of the sedimentary trench fill and hence the geometry of the top of the downgoing plate. Sedimentary velocities and basement depth were then held fixed in the following iterative inversions. The oceanic crust was inverted using P_g and P_mP phases in order to derive the velocity field and Moho depth, and similarly, the crustal velocities and Moho depth remained fixed for the next inversion. Finally, the upper mantle velocities were inverted using P_n phases. The applied hybrid scheme uses both first and second arrivals to constrain the velocity model, without the need to disregard for example secondary arrivals such as lower crustal P_g phases which become secondary arrivals where P_n arrivals overtake P_g .

[12] Horizontal grid spacing of the model used for the velocity inversion is 0.5 km, whereas the vertical grid spacing is varied from 0.05 km at the top of the model to 0.5 km at the bottom.

Depth nodes defining the reflectors are spaced at 2 km. We used horizontal correlation lengths ranging from 2 km at the top to 10 km at the bottom of the model, and vertical correlation lengths varying from 0.4 km at the top to 2.5 km at the bottom. Depth and velocity nodes are equally weighted in the joint refraction and reflection traveltime inversion.

4.1. Sedimentary Section Tomography

[13] Seaward from the trench, the basement was derived by picking and converting the vertical incidence reflections from two-way-time (TWT) data to depth using a constant velocity of 1.7 km/s. Approaching the trench (up to profile distance km 200), a 2-km deep trench basin has been developed with incoming pelagic sediments and turbidites (Figure 2b). Here, refracted P_s phases and reflected P_bP phases (Figure 3e) were used to invert the velocity structure of the sediments in the trench and the top of the oceanic crust. The starting model for the sedimentary trench fill and lower continental slope is shown in Figure 4a and was set up using the semi forward modeling approach of Zelt and Smith [1992]. The starting model includes the known bathymetry; the velocity at the top of the sedimentary layer is set to 1.7 km/s. Below the seafloor the velocity varies depending on the depth using a constant vertical velocity gradient of 1 s^{-1} . The starting reflector is directly computed by converting the TWT data of the corresponding basement reflector to depth. For this reference model, the initial root-mean square (RMS) travel-time misfits for P_s and P_bP are 407 ms and 567 ms, respectively. As the crustal phases were omitted in this step, the input model still contains sedimentary velocity below the sediment-crust boundary (Figure 4a).

[14] Tests with several starting models converge to nearly the same final model. In order to study the accuracy of the final model, we employed the Monte Carlo method [e.g., Korenaga *et al.*, 2000]. The uncertainty of a nonlinear inversion can be expressed in terms of the posterior model covariance matrix [e.g., Tarantola, 1987], which can be approximated by the standard deviation of a large number of Monte Carlo realizations assuming that all the realizations have the same probability [e.g., Tarantola, 1987]. The uncertainty estimated by this method should be interpreted as the uncertainty for our model parameters (i.e., starting velocity model and smoothing constraints). The procedure to estimate velocity uncertainties con-

sisted of randomly perturbing velocities of our reference model (Figure 4a). We generated 100 random initial velocity models by adding smooth perturbations randomly distributed (maximum velocity perturbations of $\pm 0.1 \text{ km/s}$ at the top and $\pm 0.4 \text{ km/s}$ at the bottom of the model, with wavelength perturbations of 5 km horizontally and 0.5 km vertically). The basement reflector depth was found by converting the TWT data of the reflector into depth using the velocity distribution of every initial model. In addition to the perturbed reference models we produced 100 so-called noisy arrival time sets constructed by adding random phase errors ($\pm 50 \text{ ms}$) and common receiver errors ($\pm 50 \text{ ms}$) to the original data set [Korenaga *et al.*, 2000]. Then we performed a tomographic inversion for each velocity model with one noisy data set, in order to estimate not only the dependence of the solution on the reference model but also the effect of phase arrival time picking errors. The mean deviation of all realizations of such an ensemble is considered to be a statistical measure of the model parameter uncertainties [e.g., Tarantola, 1987]. All of the Monte Carlo inversions converged in less than 10 iterations to $\chi^2 = 1$, where χ^2 is the normalized sum of the RMS misfits divided by the corresponding picking uncertainties; a value of 1 means that the model error is equal to the data uncertainty. Figure 4b shows the average model from the 100 final models. The RMS error was reduced to $\sim 50 \text{ ms}$ for refractions and $\sim 55 \text{ ms}$ for reflections. Figure 4c shows the derivative weight sum (DWS), which is a statistical parameter indicating the model resolution and ray density. The standard deviation of the calculated velocities for most of the model is below 0.1 km/s and for the reflector depth $< 0.1 \text{ km}$, except at the eastern edge of the model (Figure 4d) where the velocity uncertainty increases to values larger than 0.2 km/s and for the depth uncertainty to values of $\sim 0.3 \text{ km}$ due to the reduced data coverage.

4.2. Oceanic Crust Tomography

[15] For the determination of the crustal part of the velocity model we held the previously determined sedimentary section fixed by using spatial damping [Korenaga *et al.*, 2000]. We inverted the oceanic crust by including all crustal phases (first and later arrivals) to their maximum offset, and the depth of the floating reflector (Moho) was identified using the mantle phases P_mP simultaneously in the tomographic inversion [Korenaga *et al.*, 2000]. As with the inversion of sedimentary layer, we use the Monte Carlo scheme for determining the

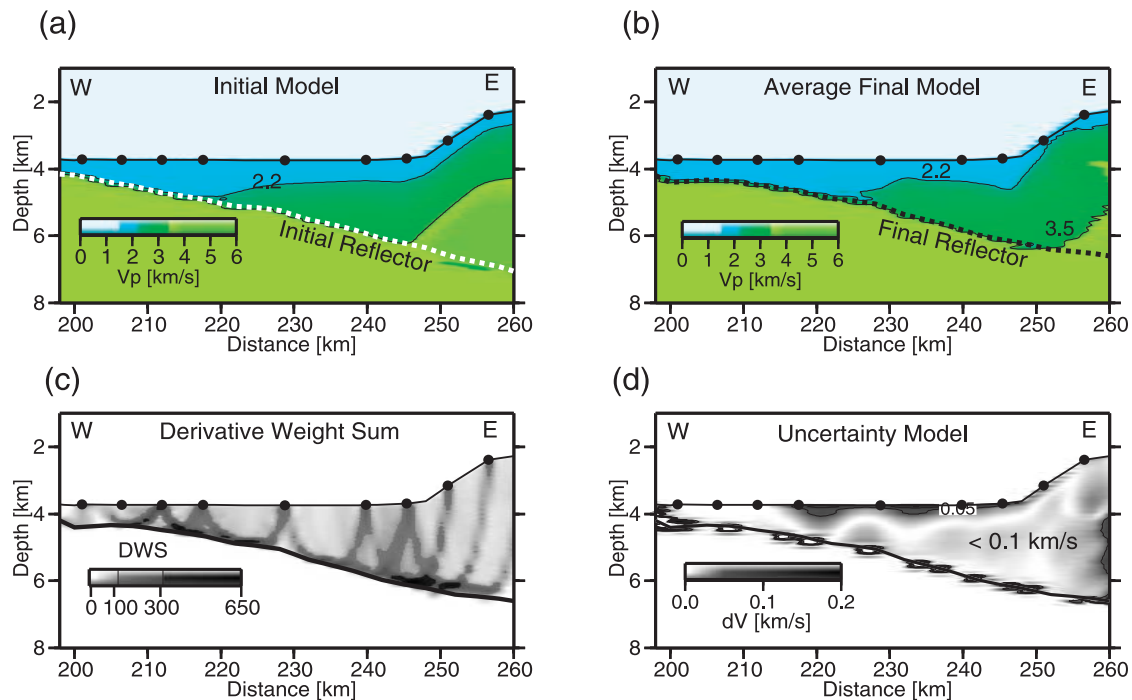


Figure 4. Result of sedimentary tomographic inversion using P_s and P_bP phases, and reflection data. (a) Initial velocity model used as a reference for the Monte Carlo analysis and for velocity inversion. (b) Final average model of the Monte Carlo ensembles. (c) Derivative Weight Sum (DWS) for rays traveling throughout model shown in Figure 4b. (d) Velocity depth uncertainty model after Monte Carlo type realizations.

crust velocities and thicknesses, and therefore a suite of starting models was required.

4.2.1. Reference Model

[16] The 2-D starting velocity models were obtained by hanging 1-D crustal velocity profiles beneath the basement (see Figure 5c). The reference 1-D velocity depth model was composed of oceanic upper crust (layer 2) and the lower crust (layer 3). Minimum values for top, mid, and bottom velocities were 3.0, 6.0, and 6.5 km/s, while corresponding maximum values were 5.0, 7.0, and 7.5 km/s, respectively. The upper crustal thickness could vary from 1 to 3 km, and the lower crustal thickness could vary from 3 to 5 km. The initial geometry of the Moho boundary was chosen as the sum of the obtained smoothed basement geometry in the previous sedimentary modeling and a given crustal thickness, which allowed variations between 4 and 8 km. Different tests showed that variation of the starting model within this model space did not affect significantly the solution. Figure 5a shows the final velocity model derived by averaging all Monte Carlo ensembles.

4.2.2. Model Uncertainty, Monte Carlo-Type Analysis

[17] Velocity and Moho-depth uncertainties of the model parameters in the oceanic plate were estimated by performing a Monte Carlo-type analysis [e.g., Tarantola, 1987], as we described above. Figure 5c shows the area covered for the 100 initial two-layer crustal velocity profiles and the 100 starting Moho reflectors underneath the basement.

[18] Initial RMS traveltimes misfits were generally higher than 900 ms, and χ^2 was initially greater than 100. The stopping criterion for each inversion was $\chi^2 \sim 1.0$, which was reached typically after 5 iterations. Using the 100 realizations, the final average crustal velocity model and its standard deviation were computed (Figure 5d). The standard deviation of the velocities is lower than 0.1 km/s in the upper crust and the main part of the lower crust as well, increasing to values of 0.1–0.15 km/s in the deepest region of the lower crust. Velocity and Moho depth uncertainties are larger at the western edge of the model where the ray coverage is poor. Moho depth uncertainties in the middle of the model are as low as 0.15 km and reach 0.4 km at

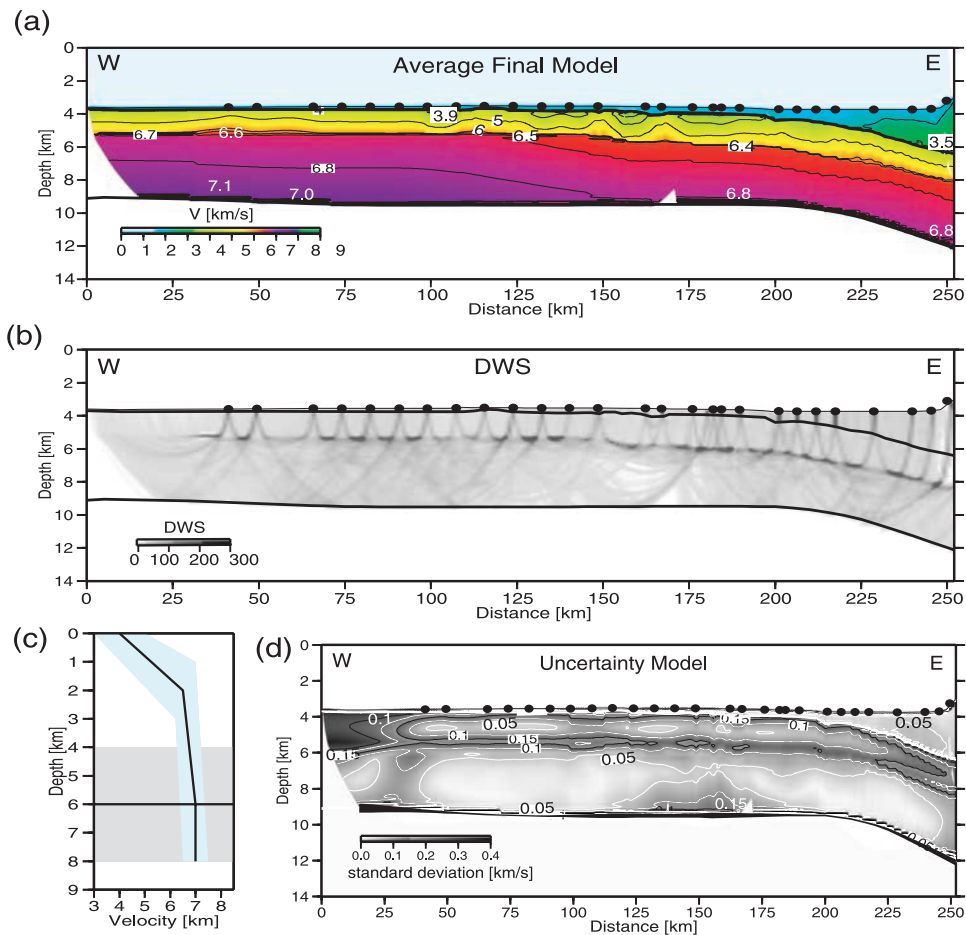


Figure 5. Result of crustal tomographic inversion using P_g and P_mP phases. (a) Final velocity model derived by averaging all Monte Carlo ensembles. (b) Derivative weight sum. (c) Range of parameters for Monte Carlo ensembles. A starting model consists of a 1-D crustal velocity profile; the Moho depth is the sum of the previously obtained smoothed basement and a given crustal thickness. Gray and light blue regions show possible variations in Moho depth and velocity randomization, respectively. (d) Corresponding standard deviation for velocity and depth nodes; contour interval is at 0.05 km/s.

the edges of the velocity model. At the trench, velocities and Moho depth are well constrained with the inclusion of stations on the continental slope [Scherwath *et al.*, 2006b]. The DWS for the model is shown in Figure 5b, which shows excellent ray coverage.

4.2.3. Resolution Test

[19] To check the resolvability of the obtained velocity model, in particular the anomalous low-velocity zones in the trench–outer rise region (Figure 5a), we have created a synthetic model consisting of four sinusoidal anomalies located in the oceanic crust (see Figure 6a), which are superimposed onto the final average velocity model. The maximum amplitude of each Gaussian anomaly is $\pm 6\%$ (Figure 6). Synthetic traveltime data with the same source–receiver geometry as in the real data set have been gener-

ated with the perturbed model, and they were inverted using an initial unperturbed model to see how well given perturbations are recovered. The recovery model is plotted in Figure 6b, which was gained after 3 iterations. The result shows that position, shape and amplitude of the velocity anomalies are reasonably well recovered within the uncertainty limits. Despite a certain deterioration in the shape of the anomalies, the result indicates that the geometry and instrument spacing yields a sufficiently high resolution for these structural anomalies, discerning between positive and negative variations along the oceanic crust. The tomographic inversion scheme used here is able to resolve structures with size and amplitude similar to the normal and low-velocity zone at this depth range. This shows that the crustal velocity reduction of the oceanic crust when approaching the trench

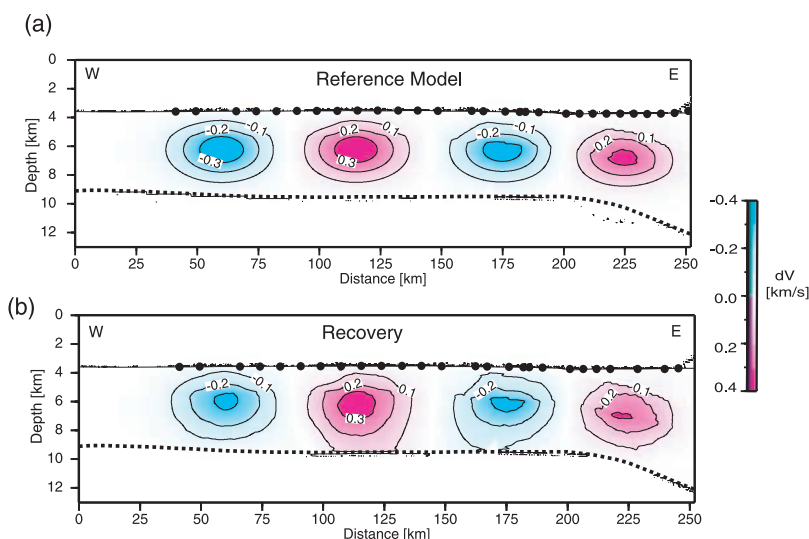


Figure 6. Results of resolution test. (a) Synthetic reference velocity model, consisting of three single sinusoidal anomalies superimposed onto the final velocity model of Figure 5a. (b) Recovery obtained after four iterations.

shown in Figure 5a is not an artifact of the seismic tomographic inversion procedure but a real feature.

4.3. Upper Mantle Tomography

[20] For the subsequent tomographic inversion of the mantle refraction P_n , a “layer-stripping” procedure was chosen, preserving the structural and velocity information above the Moho interface gained before. For the Monte Carlo inversion approach, we constructed several initial models by varying the uppermost mantle velocity between 7.5 to 8.5 km/s and the mantle velocity gradient between 0 and 0.04 s^{-1} respectively. The final average model and its uncertainties are plotted in Figure 7. The results exhibit a clear trend of velocity-reduction toward the trench, which is well correlated with the location of the outer rise but landward of the crustal velocity reduction. Uncertainties of the upper mantle velocity in the outer rise region range between 0.1–0.2 km/s and are well constrained in the seaward part (~ 0.1 km/s) where the plate geometry is relatively flat and the sediments are thin.

[21] To survey the robustness of our tomographic results, we conducted independent forward modeling seeking a minimum-structure model that satisfies the data. Model features common to the tomographic and forward-modeling output may be assessed without using subjective a priori information [e.g., Zelt and Smith, 1992]. We studied uppermost mantle velocity and different velocity gradients by keeping the structural and velocity information above the Moho interface gained for the crustal tomography (Figure 5a). Figure 8a

shows the record section of OBH 68, which displays an example of the onset of the P_g , P_mP and P_n phases. “Normal” crustal velocities fit the crustal phases well, and the best-fitting uppermost mantle velocity is about 8.3 km/s. A comparison with a reduced upper mantle velocity of 8.0 km/s produces a large P_n traveltime misfit (Figure 8a), and so we conclude that the seismic data can only be explained with uppermost velocities as fast as 8.3 km/s. Toward the trench the situation changes; a “delay” of P_n arrivals is observed (Figure 8b). These delayed P_n arrivals are already apparent in most of the trenchward branches of seismic stations. A large amount of the total delay in P_n arrivals can be attributed to the thick sedimentary sequence, which covers the deflected downgoing plate (see Figure 4b). However, as our previous sedimentary tomography constrains the sediment structure, a remaining delay of 150 ms is still required to fit P_n arrivals within the uncertainty of the picked arrivals. A better P_n traveltime fit occurs with uppermost mantle velocities ranging between 7.7–8.0 km/s. We also plotted the predicted traveltimes for P_n with an uppermost mantle velocity of 8.2 km/s; the arrivals are predicted up to 150 ms earlier than observed (Figure 8b). In conclusion, the high-quality P_n phases clearly define a reduction of upper mantle velocities toward the trench.

5. Discussion

[22] The data presented in this paper show systematic changes of crustal and upper mantle seismic

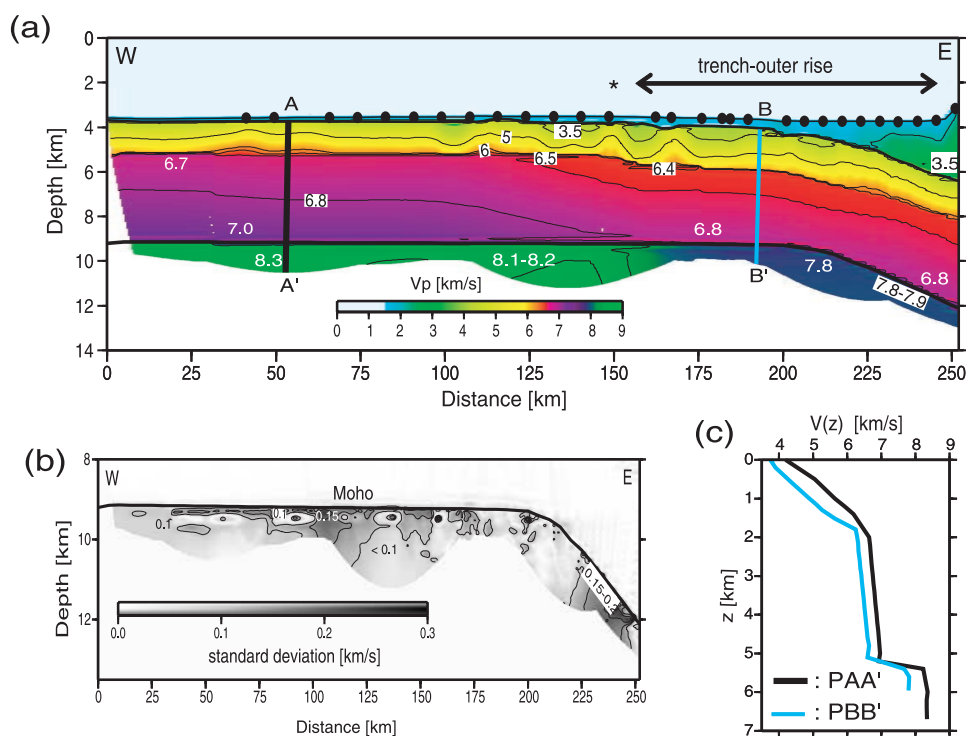


Figure 7. Result of mantle tomographic inversion using refracted P_n phases. (a) Final velocity model derived by averaging all Monte Carlo ensembles (see text for details). (b) Corresponding standard deviation for upper mantle velocity model; contours are drawn at 0.05 km/s interval. Velocity uncertainty is higher between $x = 220$ –250 km below the thick sediments at the trench. (c) Comparison of velocity depth structure for extracted profile from our velocity model shown in Figure 7a. Black line shows velocity structure $V(z)$ away from the trench, and blue line shows $V(z)$ beneath the trench–outer rise.

structure in the form of velocity reduction in the oceanic Nazca plate while it approaches the Chile trench. In this section, we discuss the transition from “normal” to deformed and altered oceanic subducting lithosphere and its possible causes within the geodynamic framework.

5.1. Seismic Structure of the Oceanic Lithosphere

5.1.1. Sediments and Basement Topography

[23] Seaward from the trench (>200 km) the southern Nazca plate is covered by a thin sequence of pelagic and hemipelagic sediments (<150 m). Here, high-resolution multibeam bathymetric mapping shows the typical topographic pattern of the tectonic fabric formed at the spreading center, which is obscured toward the trench due to turbidites deposits (Figure 2b). From profile km $x \sim 50$ to 200, turbidites fill the half-graben structure and overlay pelagic sediments, forming a mix-sedimen-

tary sequence of 200–400 m thickness. Further to the east (in the trench basin), the sedimentary-cover becomes thicker, resulting in a total thickness of $\sim 2,000$ m (Figure 4b). Trench sediments were mainly delivered during the Pleistocene glaciation with a rapid sedimentation rate [Bangs and Cande, 1997]. At the bottom of the trench basin, compressional velocities of 3.0–3.5 km/s were detected at 2 km-depth below seafloor. These velocities are because of compaction processes and the increase of sediment size from top to bottom (graded bedding), associated to sedimentary deposit events.

[24] The basement topography is in general rough, and it is characterized by the presence of outcrops of basement highs (Figure 2a). In the outer-rise ($x \sim 150$ km), and approximately 5 km to the north of the seismic profile a basement outcrop rises ~ 200 m above the surrounding seafloor (Figure 9a), while its associated basaltic edifice rises ~ 400 m above regional basement. Ten kilometers to the north of this basement outcrop, several abyssal hills generated at the spreading

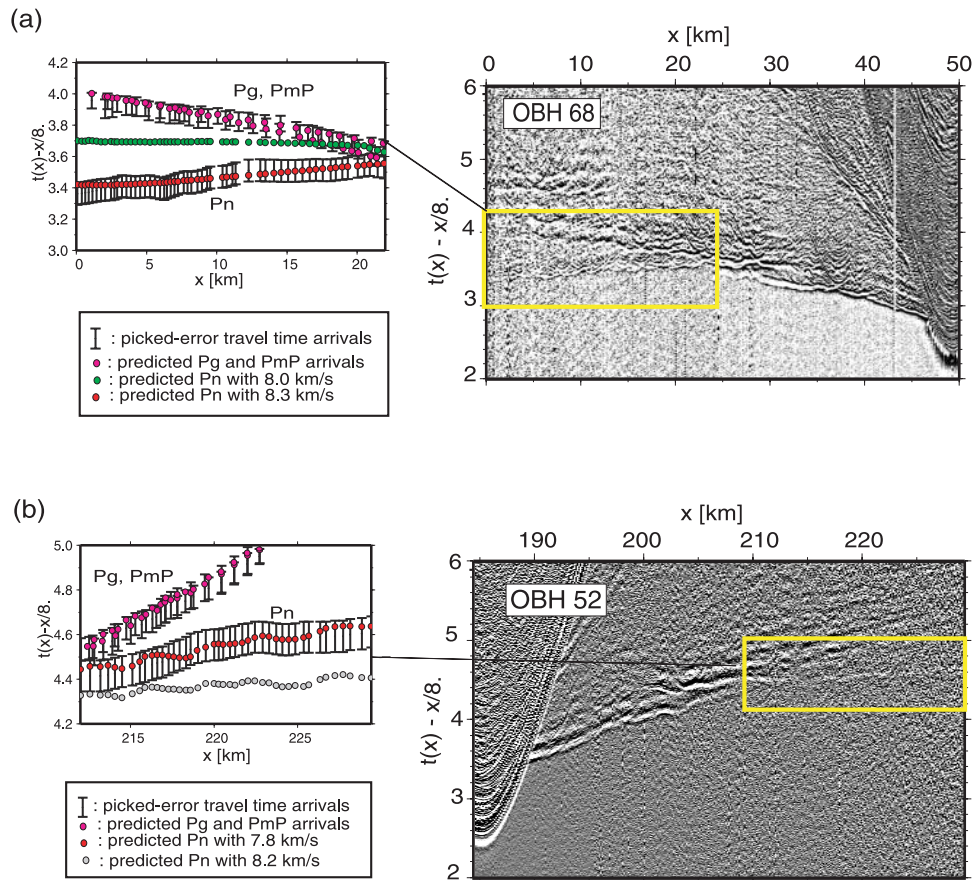


Figure 8. Detailed forward analysis of P_n traveltimes for (a) oceanward branch of OBH 68 and (b) trenchward branch of seismic record section of OBH 52. Predicted P_g and P_{mP} arrivals are based on the final crustal model shown in Figure 5a. (a) P_n oceanic phases can only be predicted with values as fast as 8.3 km/s (red dots); uppermost velocities values of 8.0 km/s produce a misfit >250 ms (green dots). (b) P_n arrivals are predicted up to 150 ms earlier than observed using an uppermost velocity of 8.2 km/s (gray dots); a better P_n traveltime fit occurs with uppermost mantle velocity of 7.8 km/s (red dots).

center with pervasive faulting and large offsets strike approximately parallel to the trench axis (Figure 2a). This area is characterized by pervasive normal faults exposing basement caused by plate bending. Southward and trenchward of the seismic profile, this fault pattern is not visible on the multi-beam bathymetry owing to the thicker sedimentary cover. Under the trench fill, however, multichannel data reveal that as the plate approaches the trench, basement topography becomes rougher and the oceanic crust is probably pervasively fractured due to bending-related faulting (Figure 2b).

5.1.2. Oceanic Crust

[25] Two distinct zones of the oceanic crust can be identified in the final model: (1) the oceanward section, away from the trench, and (2) the trench–outer rise region just prior of the subduction of the oceanic plate. Figure 7c compares the velocity

structure beneath the sediments for well resolved velocity-depth profiles of zones 1 and 2.

[26] In the oceanward section of the velocity model, the velocity structure below basement roughly follows the basement topography. Velocities in the ~ 1.7 km thick layer are between 4.0–4.2 km/s at the top and ~ 6.6 km/s at the bottom and correspond to oceanic layer 2; a typical sequence of extrusive basalts on top of a sheeted dike complex and high velocity gradient of about 1.4 s^{-1} . Both seismic velocity and gradient are similar to the seismic structure obtained off-axis in the upper crust of the southern East Pacific Rise [Grevemeyer *et al.*, 1998]. These values are in good agreement with mature oceanic crust sufficiently far way from the ridge crests so that strong hydrothermal circulation has largely ceased [Grevemeyer *et al.*, 1999]. Layer 2 overlies a ~ 3.6 km thick layer with velocities increasing from 6.6 km/s to ~ 7.0 – 7.1 km/s. This

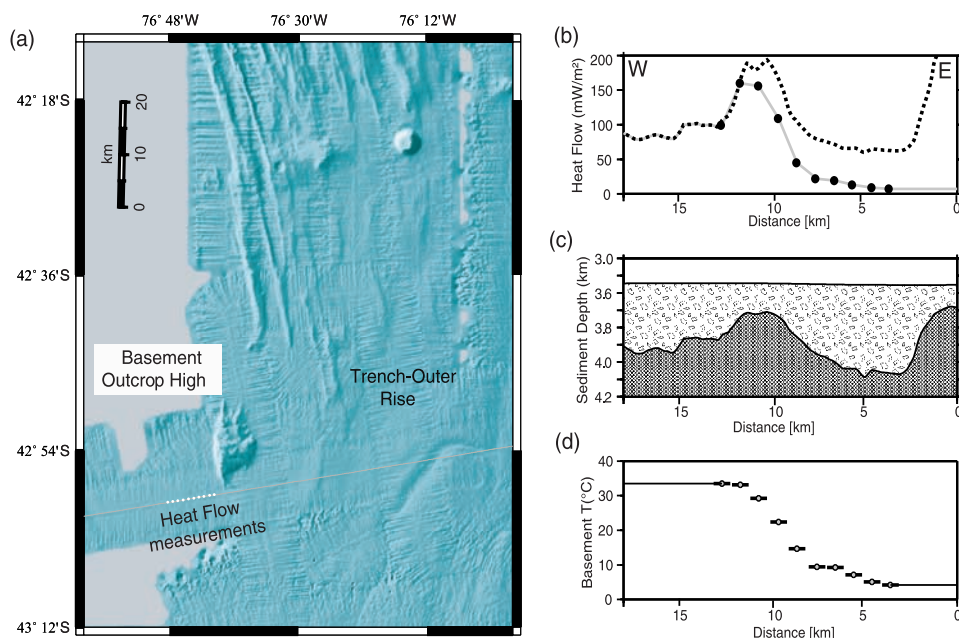


Figure 9. (a) Location of heat flow stations along seismic profile. (b) Heat flow measurements (black dots). Predicted heat flow values using a basement temperature of $T_b = 40^\circ\text{C}$ (dotted line). Predicted heat flow values incorporating hydrothermal cooling (gray line). (c) Basement topography obtained from seismic reflection data. (d) Temperature distribution at the basement used in our heat flow model with cooling. For Figures 9b, 9c, and 9d, distance is measured from the location of the basement outcrop high.

seismic structure is typical of oceanic layer 3 normally associated with gabbro and layered gabbro rocks (layer 3A and 3B) [e.g., Vera *et al.*, 1990]. The velocity range of 6.6–7.1 km/s is consistent with lower crust relative anhydrous in composition, which is typical for oceanic crust formed at fast spreading ridges [e.g., Carbotte and Scheirer, 2004; Karson, 1998]. The bulk porosity of the crust should be rather low due to the closure of cracks and fissures by hydrothermal mineralization [e.g., Grevemeyer and Bartzeko, 2004].

[27] Approaching the trench, velocities for the igneous crust start to decrease 100 – 150 km from the deformation front (Figure 5a). The uppermost crustal velocities decrease to values lower than 3.7 km/s (Figure 7c), which are much lower than typical uppermost layer 2 velocities of mature oceanic crust (>4.5 km/s) [Carlson, 1998; Grevemeyer and Bartzeko, 2004]. Lowermost crustal velocities decrease to values lower than 6.9 km/s (Figure 5a), implying the likely presence of hydrous minerals, such as chlorite and amphibolites [e.g., Hess, 1962; Christensen and Salisbury, 1975]. The decrease of velocities is accompanied with an increase in roughness of the basement topography, and probably coincides with activation of new cracks and normal extensional faults induced by plate bending [e.g.,

Ranero and Sallares, 2004]. This process suggests a significant alteration of the porosity structure of the entire subducting oceanic crust.

[28] Moho reflections (P_mP) constrain the transition from “crustal” gabbros to “mantle” ultramafic rocks, which occurs at ~ 5.3 km depth below the top of the basement. Crustal thickness is therefore less than the average value of 6.48 ± 0.75 km reported by White *et al.* [1992] for Pacific crust younger than 30 Ma. McClain and Atallah [1986], however, estimated that Pacific crust averages 5.67 ± 0.88 km for crust of the same age, and Walter *et al.* [2000] and Grevemeyer *et al.* [2007] found in more recent studies that crust of the Cocos plate is 5.0–5.5 km thick.

5.1.3. Uppermost Oceanic Mantle

[29] Seaward from the trench, compressional velocity of 8.3 km/s was detected in the uppermost 2–2.5 km of the mantle (Figure 7a). Typical mature oceanic mantle velocities are faster than 8.1 km/s, which is usually associated to an anhydrous composition of mantle peridotite [e.g., Peacock, 1990]. Thus oceanic Nazca plate approaches the subduction zone with a mantle comparatively undeformed and dry (Figure 7a). Closer to the trench, however, a progressive velocity-reduction in the upper mantle

occurs. The velocity reduction is visible ~ 80 km from the deformation front (Figure 7a), and they decrease to minimum values of ~ 7.8 km/s, which is significantly lower than the velocity of mantle peridotite (> 8.1 km/s). P_n phases image only the first ~ 2 km of the uppermost mantle in the outer rise area (Figure 7a). Thus the maximum depth of possible hydration in the mantle remains unconstrained.

[30] It has been documented that the uppermost mantle velocity reduction is even larger in poorly sedimented margins. In north Chile, for example, upper-mantle velocities in the trench–outer rise area reach values as low as 7.6 km/s [Ranero and Sallares, 2004]. Offshore of Costa Rica, seismic velocities under the trench at the Moho are even lower (7.3–7.4 km/s), with velocities increasing to ~ 7.5 –7.8 km/s at about 3–4 km below the Moho [Grevemeyer et al., 2007]. Offshore of south central Chile, upper mantle velocity reduction is slightly lower and solely restricted to the trench–outer rise area (Figure 7a), where bending-related faulting is suggested to lead to hydration of the upper mantle [Ranero et al., 2003]. Since water is required to alter mantle peridotite to serpentinite, pervasive fracturing of the entire crust is suggested for the lithosphere entering the Chilean subduction zone offshore Chiloe Island.

5.2. Water Pathways

[31] The efficiency of fluid percolation depends on the sedimentary thickness and faulting history. Faults constitute the possible water pathways but they can be blocked by insulating sediments. Therefore slab hydration prior to subduction is believed to be largest where outcropping basement relief facilitates the flow of seawater into the crust [Grevemeyer et al., 2005]. The abyssal hill fabric inherently related to the formation process of the oceanic lithosphere at the mid-ocean ridge is well imaged just 5 km to the north of the seismic line (Figure 2a). Therefore reactivation of fractures by bending-related normal faulting in this region might be an important mechanism for plate hydration.

[32] High-resolution seismic data provides evidence for some extensional faults reflected by offsets in the trench–outer rise region (Figure 2b), suggesting the trenchward increase of fracturing intensity. This indicates that the bending-related faulting is active in the outer rise, and it fractures the oceanic crust beneath the sedimentary bed. High-resolution multibeam bathymetry shows,

though, that surface-cutting faults are not visible on the seafloor along this profile (Figure 2a). As the insulating sediments are several hundreds of meters thick (Figure 2b) an efficient inflow of seawater is unlikely to explain the reduced velocities in the outer rise. However, the onset of velocity reduction in the oceanic crust is well correlated with the location of an outcropping basement high or seamount (Figures 7a and 9), suggesting a relationship between plate hydration and basement outcrop. Seamounts or basement highs provide the necessary pathways to move huge volumes of fluid through oceanic crust over large distances, even when the crust is insulated by thick sediments [Fisher et al., 2003a, 2003b].

[33] In order to study the hydrothermal activity in the outer rise, we have directly measured heat flow values on the outer bulge offshore of Chiloe Island [Flueh and Grevemeyer, 2005]. Figure 9a shows the location of 10 heat flow stations immediately at the seaward flank of the basement outcrop (see also the bathymetry in Figure 2a). The heat flow values decrease from 100–150 to ~ 7 mW/m² over a distance of less than 10 km toward the trench (Figure 9b). We computed two predicted heat flow models using two different temperature distributions at the top of the igneous basement. In the first model basement temperature is isothermal. In the second model basement temperatures varies as a function of distance from the basement high and hence mimics cooling by inflow of cold seawater. Crucial parameters are the temperature at the basement T_{bas} and at the seafloor T_{sea} , and the thermal conductivity structure k between the basement and the seabed. We use a linear temperature gradient and the simple conductive heat transport relation

$$q = k \, dT/dz$$

where q is the heat flow, $dz = z_{bas} - z_{sea}$ is the thickness of the sediments, and $dT = T_{bas} - T_{sea}$. The sedimentary thickness comes directly from the high-resolution reflection data and is plotted in Figure 9c. The seafloor temperature is assumed $T_{sea} = 0^\circ\text{C}$, and thermal conductivity k was measured in situ. Testing with different $T_{bas}(x)$ distributions, the extreme low values toward the trench can only be predicted by the cooling model (Figures 9b and 9d). This finding suggests a very efficient inflow of cold seawater into the oceanic crust through the basement outcrop feature located just 5 km north of the profile.

[34] The flanks of the high outcrop basement probably act as an important and primary entry of cold seawater into the igneous oceanic crust. This process accompanied by the opening of new cracks and activation of extensional faults due to bending-related faulting increases the permeability and hence facilitates a deeper fluid inflow, probably, reaching mantle depths, as supported by our tomographic results (Figure 7a). We see a number of other mounds and basement ridges imaged in the multibeam bathymetry to the north of the profile, which may act as recharge and discharge sites and therefore fuel a hydrothermal circulation in the outer rise. Cold seawater might be transported laterally between separated basement outcrops for distances of more than 50 km [Fisher *et al.*, 2003a], which implies that fluids may circulate through most of the studied trench–outer rise area. Here, bending-related faulting might increase the permeability of the oceanic crust, and consequently facilitates and reactivates hydrothermal circulation.

[35] Moreover, the incoming plate may laterally carry water already percolated in the oceanward part of the outer rise (70–40 km from the trench axis), where plate bending is strongest, igneous basement is more exposed, and due to a higher water/rock ratio hydration might be more vigorous. In this part of the outer rise, the sedimentary thickness is comparable with the outer rise in Middle America (200–400 m thick), which is highly hydrated [Ranero *et al.*, 2003]. Once cold seawater is stored in cracks and/or faults and faulting continues toward the deformation front, water trapped within the crust may migrate deeper where larger faults cut into the mantle.

5.3. Volatiles Stored in the Oceanic Subducting Lithosphere

[36] The amount of volatiles stored in the subducting oceanic lithosphere consists mainly of three components: volatiles stored (1) in subducting sediments, (2) in the oceanic crust, and (3) in the oceanic mantle. Recent studies, however, suggest that most of the bound water enters subduction zones within the oceanic crust and mantle [Peacock, 1990; Ranero *et al.*, 2003].

[37] The observed crustal velocity reduction beneath the trench–outer rise is caused in part by cracks and fissures induced by plate bending. The similar trend for upper and lower crustal velocities has been observed in the northern Chile trench, which was explained as consequence of fracturing rather than hydration [Ranero and Sallares, 2004].

The amount of chemically bound water in the crust is therefore not straightforward to estimate by the magnitude of velocity reduction. Peacock [1990] concludes from chemical analysis of drill cores of oceanic crust that a 2.5-km-thick basaltic layer contains in average 2 wt.% H₂O and ~0.1 wt.% CO₂, and a 3- to 5-km-thick oceanic gabbro layer contains roughly 1% H₂O and ~0.1 wt.% CO₂. Hacker *et al.* [2003] calculated a maximum water content of 1.3 wt% H₂O for partially hydrated lower oceanic crust based on a global compilation of physical properties of minerals. Carlson [2003] shows that, based on the modal mineralogy and seismic properties of oceanic diabase and gabbro samples, gabbros with velocities typical for the lower oceanic crust (6.7–7.0 km/s) already contain a mean water content near 0.5 wt%. This value could be much larger if lower oceanic crust has been altered by tectonic processes, as is probably the case in our study area.

[38] Quantifying the amount of serpentine in subducting oceanic mantle is also difficult because relatively modest amounts of serpentine can represent a major H₂O input into the subduction factory [Peacock, 2001]. Following Carlson and Miller [2003], an approximate formula to estimate water content in the partially-serpentinized peridotites is $w(\%) \approx -0.33\Delta V$, where w is the water content (in weight percentage) and ΔV is the percent difference between the observed velocity and the velocity in unaltered peridotite. The upper mantle P wave velocity in our study region ranges between 7.8 to 8.3 km/s, corresponding to serpentinite contents of roughly 0 to 9%; and the corresponding range of water contents of 0 to 3.0% (0 to 4 moles/m³). These values are lower compared to estimates in Central America (>20% of serpentinization) [Ranero *et al.*, 2003], the erosional margin in northern Chile (~17% of serpentinization) [Ranero and Sallares, 2004], and offshore Costa Rica (10–25% of serpentinization) [Grevemeyer *et al.*, 2007]. Nevertheless, the total amount of hydration and thus the total volume of fluids entering the subduction zone in south central Chile should be larger than the 9% bound in the upper mantle because of the volatile stored in the entire oceanic crust plus subducting sediments. Moreover, this degree of hydration can be even larger if the oceanic plate continues to hydrate during subduction [Ranero *et al.*, 2003].

6. Conclusions

[39] Joint inversion of seismic refraction and wide-angle data offshore of south-central Chile yields

the P wave velocity structure of the subducting oceanic Nazca plate. This information and the tectonic features obtained from high-resolution seismic data, multibeam bathymetry and heat flow measurements suggest that the structure of the incoming plate changes systematically within ~ 120 km off the trench axis as the lithosphere approaches the deep-sea trench. This work leads to the following conclusions:

[40] 1. The 2-D velocity model derived from tomographic traveltime inversion consist of a ~ 5.3 km thick oceanic crust and shows a classical mature fast spreading P wave velocity structure in the seaward part outside of the influence of plate bending at the trench–outer rise. Seismic analysis of P_n arrivals reveals fast uppermost mantle velocities of ~ 8.3 km/s, >120 km seaward of the trench. The velocity structure found in this zone indicates that the oceanic lithosphere is relatively dry and undeformed.

[41] 2. Approaching the Chile trench, seismic velocities decrease, indicating an evolutionary process changing the structure of the lithosphere, likely to be related to an increase in fracture porosity and hydration of both the oceanic crust and the uppermost mantle. Reduced velocities are only located in the trench and outer-rise area. The decrease of velocities is accompanied by an increase of basement-relief roughness and also by the amount of stress induced by the plate bending.

[42] 3. In spite of the thick sedimentary blanket on the incoming plate, an efficient inflow of cold seawater into the oceanic crust through outcropping basement highs or seamounts is supported by anomalously low heat flow values, which are spatially well correlated with the onset of velocity reduction in the crust and upper mantle. Cold seawater might be laterally transported between high basement outcrops over large distances (>50 km) in the vicinity of the trench–outer rise area. This primary water pathway could extend to mantle depth through bending induced trench parallel normal faults, and thus cause a hydration of the upper mantle.

[43] 4. Assuming that the mantle velocity reduction is produced only by hydration, serpentinization of the uppermost mantle from the outer rise to the trench axis is $\sim 9\%$ in the uppermost 2 km of the mantle, where seismic data provide enough resolution. This degree of hydration in the uppermost mantle is about 10% less than observed in poorly sedimented margins.

[44] In summary, seismic data of high resolution reveal a clear alteration of the oceanic lithosphere at the outer rise just prior to its subduction, showing that the alteration occurs where strong plate bending is likely to modify the large scale porosity and permeability structure of oceanic lithosphere, and simultaneously nurtures the migration of cold seawater through crustal faults down to mantle depth, resulting in hydration of both oceanic crust and upper mantle. Infiltration of cold seawater, and consequently hydration of the subducting oceanic lithosphere may also occur at heavily sedimented trenches through high base-ments outcrops where igneous crust is exposed.

Acknowledgments

[45] We are grateful to Masters Kull and Mallon and their officers and crew of R/V *Sonne* and all scientists who assisted in data collection during cruise SO181. This is publication GEOTECH-276 of the R&D-Programme GEOTECHNOLOGIEN funded by the German Ministry of Education and Research (BMBF) and German Research Foundation (DFG), grants 03G0181A, 03G0594E, and 03G0594F. One of the authors (E.C.-R.) gratefully acknowledges a scholarship granted by the German Academic Exchange Service (DAAD).

References

- Alt, J. C., J. Honnorez, C. Laverne, and R. Emmermann (1986), Hydrothermal alteration of a 1 km section through the upper oceanic crust, Deep Sea Drilling Project Hole 504B: Mineralogy, chemistry, and evolution of seawater–basalt interactions, *J. Geophys. Res.*, **91**, 10,309–10,335.
- Angermann, D., J. Klotz, and C. Reigber (1999), Space-geodetic estimation of the Nazca–South America Euler vector, *Earth Planet. Sci. Lett.*, **171**(3), 329–334.
- Bangs, N. L., and S. C. Cande (1997), Episodic development of a convergent margin inferred from structures and processes along the Southern Chile margin, *Tectonics*, **16**, 489–503.
- Bialas, J., and E. R. Flueh (1999), Ocean bottom seismometers, *Sea Technol.*, **40**(4), 41–46.
- Carbotte, S., and D. S. Scheirer (2004), Variability of ocean crustal structure created along the global mid-ocean ridge, in *Hydrogeology of Oceanic Lithosphere*, edited by E. E. Davis and H. Elderfield, pp. 128–150, Cambridge Univ. Press, New York.
- Carlson, R. L. (1998), Seismic velocities in the uppermost oceanic crust: Age dependence and the fate of layer 2A, *J. Geophys. Res.*, **103**(B4), 7069–7078.
- Carlson, R. L. (2003), Bound water content of the lower oceanic crust estimated from modal analyses and seismic velocities of oceanic diabase and gabbro, *Geophys. Res. Lett.*, **30**(22), 2142, doi:10.1029/2003GL018213.
- Carlson, R. L., and D. J. Miller (2003), Mantle wedge water contents estimated from seismic velocities in partially serpentinized peridotites, *Geophys. Res. Lett.*, **30**(5), 1250, doi:10.1029/2002GL016600.
- Chapple, W. M., and D. W. Forsyth (1979), Earthquakes and bending plates at trenches, *J. Geophys. Res.*, **84**, 6729–6749.



- Christensen, D. H., and L. J. Ruff (1983), Outer-rise earthquakes and seismic coupling, *Geophys. Res. Lett.*, **10**, 697–700.
- Christensen, N. I., and M. H. Salisbury (1975), Structure and constitution of the lower oceanic crust, *Rev. Geophys.*, **13**, 57–86.
- Fisher, A. T., C. A. Stein, R. N. Harris, K. Wang, E. A. Silver, M. Pfender, M. Hutnak, A. Cherkaoui, R. Bodzin, and H. Villinger (2003a), Abrupt thermal transition reveals hydrothermal boundary and role of seamounts within the Cocos Plate, *Geophys. Res. Lett.*, **30**(11), 1550, doi:10.1029/2002GL016766.
- Fisher, A. T., et al. (2003b), Hydrothermal recharge and discharge across 50 km guided by seamounts on a young ridge flank, *Nature*, **421**, 618–621.
- Flueh, E. R., and J. Bialas (1996), A digital, high data capacity ocean bottom recorder for seismic investigations, *Int. Underwater Syst. Design*, **18**(3), 18–20.
- Flueh, E. R., and I. Grevemeyer (Eds.) 2005. TIPTEQ SONNE Cruise SO-181, from the Incoming Plate to mega Thrust EarthQuakes, *Geomar Rep.* 102, Geomar, Kiel, Germany.
- Grevemeyer, I., and A. Bartetzko (2004), Hydrothermal ageing of oceanic crust: Inferences from seismic refraction and bore hole studies, in *Hydrogeology of Oceanic Lithosphere*, edited by E. E. Davis and H. Elderfield, pp. 128–150, Cambridge Univ. Press, New York.
- Grevemeyer, I., and W. Weigel (1996), Seismic velocities of the uppermost igneous crust versus age, *Geophys. J. Int.*, **124**, 631–635.
- Grevemeyer, I., and W. Weigel (1997), Increase of seismic velocities in upper oceanic crust: The “superfast” spreading East Pacific Rise at 14°14'S, *Geophys. Res. Lett.*, **24**(3), 217–220.
- Grevemeyer, I., W. Weigel, and C. Jennrich (1998), Structure and ageing of oceanic crust at 14°S on the East Pacific Rise, *Geophys. J. Int.*, **135**, 573–584.
- Grevemeyer, I., N. Kaul, H. Villinger, and W. Weigel (1999), Hydrothermal activity and the evolution of the seismic properties of upper oceanic crust, *J. Geophys. Res.*, **104**(B3), 5069–5080.
- Grevemeyer, I., N. Kaul, J. L. Diaz-Naveas, H. Villinger, C. R. Ranero, and C. Reichert (2005), Heat flow and bending-related faulting at subduction trenches: Case studies offshore of Nicaragua and Central Chile, *Earth Planet. Sci. Lett.*, **236**, 238–248.
- Grevemeyer, I., C. R. Ranero, E. R. Flueh, D. Klaeschen, and J. Bialas (2007), Passive and active seismological study of bending-related faulting and mantle serpentinization at the Middle America trench, *Earth Planet. Sci. Lett.*, doi:10.1016/j.epsl.2007.04.013.
- Hacker, B. R., G. A. Abers, and S. M. Peacock (2003), Subduction factory: 1. Theoretical mineralogy, densities, seismic wave speeds, and H₂O contents, *J. Geophys. Res.*, **108**(B1), 2029, doi:10.1029/2001JB001127.
- Hess, H. H. (1962), History of ocean basins, in *Petrological Studies: A Volume in Honor of A. F. Buddington*, edited by A. E. Engel, H. L. James, and B. F. Leonard, pp. 599–620, Geol. Soc. of Am., Boulder, Colo.
- Kanamori, H. (1971), Seismological evidence for lithospheric normal faulting: The Sanriku earthquake of 1933, *Phys. Earth Planet. Inter.*, **4**, 289–300.
- Karson, J. A. (1998), Internal structure of oceanic lithosphere: A perspective from tectonic windows, in *Faulting and Magmatism at Mid-Ocean Ridges*, *Geophys. Monogr. Ser.*, vol. 106, edited by W. R. Buck et al., pp. 177–218, AGU, Washington, D. C.
- Korenaga, J., W. S. Holbrook, G. M. Kent, P. B. Kelemen, R. S. Detrick, H. C. Larsen, J. R. Hopper, and T. Dahl-Jensen (2000), Crustal structure of the southeast Greenland margin from joint refraction and reflection seismic tomography, *J. Geophys. Res.*, **105**, 21,591–21,614.
- McClain, J. S., and C. A. Atallah (1986), Thickening of oceanic crust with age, *Geology*, **14**, 574–805.
- Peacock, S. (1990), Fluid processes in subduction zones, *Science*, **248**, 329–337.
- Peacock, S. (2001), Are the lower planes of double seismic zones caused by serpentine dyhydration in subducting oceanic mantle?, *Geology*, **29**, 299–302.
- Peacock, S. M. (2004), Insight into the hydrogeology and alteration of oceanic lithosphere based on subduction zones and arc volcanism, in *Hydrogeology of Oceanic Lithosphere*, edited by E. E. Davis and H. Elderfield, pp. 659–676, Cambridge Univ. Press, New York.
- Ranero, C. R., and V. Sallares (2004), Geophysical evidence for alteration of the crust and mantle of the Nazca Plate during bending at the north Chile trench, *Geology*, **32**, 549–552.
- Ranero, C. R., J. Phipps Morgan, K. McIntosh, and C. Reichert (2003), Bending, faulting, and mantle serpentinization at the Middle America trench, *Nature*, **425**, 367–373.
- Reichert, C., B. Schreckenberger, and SPOC Team (2002), Fahrtbericht SONNE-Fahrt SO-161 Leg 2&3 SPOC, Subduktionsprozesse vor chile-BMBF-Forschungsvorhaben 03G0161A- Valparaiso 16.10.2001–Valparaiso 29.11.2001, Bundesanst. für Geowissenschaften und Rohstoffe, Hannover, Germany.
- Scherwath, M., E. R. Flueh, I. Grevemeyer, F. Tilmann, E. Contreras-Reyes, and R. W. Weinrebe (2006a), Investigating subduction zone processes in Chile, *Eos Trans. AGU*, **87**(27), 265–272.
- Scherwath, M., E. Contreras-Reyes, I. Grevemeyer, E. R. Flueh, W. Weinrebe, and the TIPTEQ Working Group (2006b), Structural images of the southern Chile subduction zone system offshore, paper presented at Third EGU General Assembly, European Geosciences Union, Vienna2 -7 April.
- Tarantola, A. (1987), *Inverse Problem Theory: Methods for Data Fitting and Model Parameter Estimation*, 613 pp., Elsevier, New York.
- Tebbens, S. F., S. C. Cande, L. Kovacs, J. C. Parra, J. L. LaBrecque, and H. Vergara (1997), The Chile ridge: A tectonic framework, *J. Geophys. Res.*, **102**(B6), 12,035–12,060.
- Thornburg, T. M., and D. M. Kulm (1987), Sedimentation in the Chile Trench: Depositional morphologies, lithofacies, and stratigraphy, *Geol. Soc. Am. Bull.*, **98**, 33–52.
- Thornburg, T. M., D. M. Kulm, and D. M. Hussong (1990), Submarine-fan development in the southern Chile trench: A dynamic interplay of tectonics and sedimentation, *Geol. Soc. Am. Bull.*, **102**, 1658–1680.
- van Avendonk, H. J. A., A. J. Harding, and J. A. Orcutt (1998), A two-dimensional tomographic study of the Clipperton transform fault, *J. Geophys. Res.*, **103**, 17,885–17,899.
- Vera, E. E., J. C. Mutter, P. Buhl, J. A. Orcutt, A. J. Harding, M. E. Kappus, R. S. Detrick, and T. M. Brocher (1990), The structure of 0- to 0.2-m.y.-old oceanic crust at 9°N on the East Pacific Rise from expanded spread profiles, *J. Geophys. Res.*, **95**(B10), 15,529–15,556.
- Villinger, H., I. Grevemeyer, N. Kaul, J. Hauschild, and M. Pfender (2002), Hydrothermal heat flux through aged oceanic crust: Where does the heat escape?, *Earth Planet. Sci. Lett.*, **202**, 159–170.



- Voelker, D., M. Wiedicke, S. Ladage, C. Gaedicke, C. Reichert, K. Rauch, W. Kramer, and C. Heubeck (2006), Latitudinal variation in sedimentary processes in the Peru-Chile Trench off Central Chile, in *The Andes—Active Subduction Orogeny, Frontiers in Earth Sciences*, edited by O. Oncken et al., pp. 193–216, Springer, Berlin.
- Walter, C., E. R. Flueh, C. R. Ranero, R. von Heune, and W. Strauch (2000), Crustal structure across the Pacific margin of Nicaragua: Evidence for ophiolitic basement and a shallow mantle sliver, *Geophys. J. Int.*, *141*, 759–777.
- White, R. S., and D. McKenzie (1992), Oceanic crustal thickness from seismic measurements and rare earth element inversions, *J. Geophys. Res.*, *97*, 19,683–19,715.
- Wilkins, R. H., G. J. Fryer, and J. Karsten (1991), Evolution of porosity and seismic structure of upper oceanic crust: Importance of aspect ratios, *J. Geophys. Res.*, *96*(B11), 17,981–17,995.
- Zelt, C. A., and R. B. Smith (1992), Seismic traveltime inversion for 2-D crustal velocity structure, *Geophys. J. Int.*, *108*, 16–34.